ALICE 2001-05
Internal Note/SIM
February 2001

Simulation of the response of the ALICE silicon pixel detectors

R. Caliandro[1], R. Dinapoli[1], R.A. Fini[1] and T. Virgili[2]

[1]*Sezione INFN, Bari, Italy.*
[2]*Dipartimento di Scienze Fisiche "E.R. Caianiello" dell'Università and Sezione INFN, Salerno, Italy.*

Abstract

A model for the description of the response of the pixel detectors has been applied to the two innermost layers of the ALICE ITS and has been introduced in the AliRoot standard package. The results of the simulation, including the average cluster sizes and the expected resolutions are discussed.

1 Introduction

A good simulation of the response of the pixels of the two innermost layers of the Inner Tracking System (ITS) [1] of the ALICE [2] experiment at LHC is crucial in order to understand the physical performances of the detector. In particular, the simulation allows to determine its vertex finding capability, its improvement in the momentum resolution and its ability to resolve double-hit ambiguities. Moreover, the track parameters and the two track resolution can strongly depend on the realistic estimate of the digit multiplicity and of the cluster size.

A model to simulate the response of pixel detectors has been presented and discussed in a previous note [3]. The model determines the digits (fired pixels) and also provides a clustering description. The model successfully reproduces data of the NA57 experiment, which is using pixels planes very similar to those designed for ALICE [4].

Now, the same algorithm has been implemented in the ALICE geometry and in AliRoot [5], the standard ALICE simulation and analysis package based on ROOT [6] framework. This note presents the results of this exercise.

In section 2 the main characteristics of the model are summarised. The geometry of the ALICE pixel detector (SPD) used in the present work is described in section 3. In section 4 some general information about the implementation of the model in the AliRoot framework are given. The results of the simulation are presented in section 5, together with their dependence on the track impact angles, on the parameters of the model and on the particle multiplicity. The conclusions are drawn in section 6.

2 Description of the model

The basic element of the model is the geometrical description of the pixel structure: the pixel cells are contiguous and the energy lost is deposited proportionally to the length of the track in each cell. In this way, the charge sharing between contiguous cells is well reproduced. In order to determine if a pixel is fired or not, a software threshold E_t to the energy lost E_l in a single cell is introduced.

The effect of the drift of the charge carriers was also tested in our simulation: it turns out that for the considered pixel geometry the drift contribution is fully negligible, since it is already accounted for by the introduced charge sharing effect [7].

The noise and the spatial dispersion of the thresholds are simulated by introducing a pedestal E_p, which fluctuates from event to event and from pixel to pixel with a Gaussian distribution centered at zero with a standard deviation σ. The effective energy that can give a signal in the pixel cells is then given by $E_{eff} = E_l + E_p$ and this value is compared with the software threshold E_t. A pixel can be fired only by noise if its pedestal fluctuation is larger than E_t.

The σ parameter has to be interpreted as the square root of the variance of the distribution describing the threshold dispersion in space and the variance of the distribution describing the pedestal fluctuation in time. Both these distributions are assumed to be Gaussian.

Coupling effects are also accounted for in our model and are described with the following parametrization: a fraction $F_r \cdot E_l$ ($F_r < 1$) of the energy lost in a cell is assigned to the two nearest cells in the row direction; a fraction $F_r \cdot (F_r \cdot E_l)$ is assigned to the two next cells, and so on. A different parameter (F_c) is used for the column direction. However, by comparison with experimental data it turns out that the coupling effects are negligible and the frequency of clusters with more than two pixels is well reproduced by considering the contribution of δ-rays [3].

The fired pixels are then grouped by a clustering algorithm. Diagonal pixels are also included into the cluster.

3 Description of the ALICE pixel detectors

In the following we describe the geometry of the pixel detector for ALICE (SPD) introduced in the AliRoot simulation program and used for the present work.

The basic element of the SPD is the ladder, consisting of a pixel detector matrix bonded to six front-end chips with fully independent readout. The ALICE1 chip, as reported in [8], is a matrix of 256×32 cells, each occupying an area of 50×425 μm^2. Both the readout logic and the local control functions are integrated on the chip. The detector matrix consists of 256×192 pixel cells, mostly measuring 50×425 μm^2, with a thickness of 150 μm. At the boundary between two front-end chips, there are two columns of cells having dimensions of 50×625 μm^2. The total dimension of the ladder is 1.28×8.38cm^2.

Four pixel ladders are aligned along their longer dimension to form a stave. The staves are arranged in space to form two cylindrical layers around the beam line. The first layer consists of 20 staves and has a radius of 4 cm. The second layer consists of 40 staves and has a radius of 7 cm. In layer 1 the staves are almost perpendicular to the radial direction, while in layer 2 they are tilted (turbo layout) in order to ensure that no particle can go undetected trough the openings among the staves above a momentum cutoff of 27 MeV/c [1].

4 The model in AliRoot

In fig 1 is sketched how the simulation model has been implemented in the AliRoot V.3.04 framework. As a standard procedure, the AliRoot MonteCarlo accounts for the event generation and the particle tracking in the experimental apparatus. It rules the δ-rays generation and the energy lost in the detector and its output

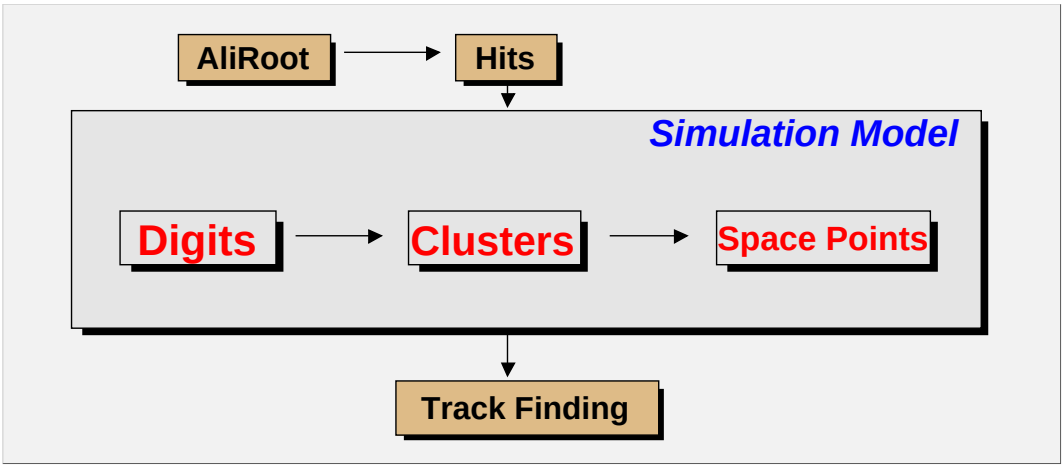

Figure 1: *Sketch of the implementation of the simulation model in AliRoot.*

consists of a set of **hits** produced by charged particles. The informations stored about each hit are: the coordinates, the track label, the track status, the energy lost by the charged particle and its momentum at the point of the hit.

These informations are used by our model to create the **digits**, namely the fired pixels in the two layers of the SPDs. As explained in section 2, the digits can be created by charge sharing, coupling or noise. In the first two cases, a track label can be associated to the digit. We allow at most three track labels to be associated to a given digit and they are sorted according to the energy they lose in the detector. This is a common feature of the three detectors in the ITS and we checked that the stored information is more than enough for the present analysis.

The digits are then grouped in **clusters**, using a simple algorithm that associates to each digit the ones present in the eight neighbouring pixel cells, if any.

As a third step, the model determines a **space point** for each reconstructed cluster. The determination of the coordinates of the space point and of the error associated to it is done separately in the two tranversal directions of the pixel plane, namely the x and z directions. If the cluster has length 1 in a given direction, the coordinate of the space point in that direction is taken as that of the center of the digit, while the error is set to (pixel length)/$\sqrt{12}$. Otherwise, if the cluster length has a length greater than 1 in a given direction, say x, the coordinate of the space point (x_{sp}) and its associated error (Δx_{sp}) are calculated according to the following expressions:

$$x_{sp} = \frac{\sum_{i=1}^{n_d}(x_d)_i}{n_d}$$

$$\Delta x_{sp} = \sqrt{\frac{\sum_{i=1}^{nd}[(x_d)_i - (x_{sp})]^2}{n_d(n_d-1)}} \qquad (1)$$

where:

$$\begin{aligned} n_d &= \text{number of digits in the cluster} \\ (x_d)_i &= \text{x coordinate of the center of the digit } i \text{ in the cluster} \end{aligned}$$

Similar expressions are used in z direction. The space points and their errors are stored in a file, together with the information on the track labels associated to them. The track label of a space point is chosen among the track labels associated to the digits of the corresponding cluster by taking the track with the higher energy lost in the detector. The association of a track to each space point, when possible, is useful to determine the resolution of the SPDs, as it will be explained in section 5.

The space points and their errors represent the inputs for the track finding procedure, which has the task of reconstructing the tracks using the informations coming from the ITS and TPC detectors.

5 Results

Particles were generated with the AliRoot internal HIJING parametrization in the angular range $10° < \theta < 170°$ and with full azimuthal angle coverage. The multiplicity in the considered θ range was set to 28000 particles, corresponding to a value of ~ 4500 charged particles per unit of pseudorapidity (η) at central pseudorapidity. The primary vertex position was set to ($x = 0$, $y = 0$, $z = 0$), without any smearing and the beam pipe was switched on. Particles were tracked through the ITS by GEANT 3.21 with all the physical effects switched on, including δ-rays production, with the threshold set to $E_\delta = 70\ keV$. The generated pseudorapidity distribution for primary charged particles and the momentum distribution of the charged particles crossing the SPD layers are shown in fig. 2.

Our model was adapted to the foreseen characteristics of the new ALICE1 chip, and the parameters were set to the following nominal values [1]:

- E_t=7.2 keV (2000 e^-);
- σ= 1 keV (280 e^-);
- F_r=0 , F_c=0.

The σ value has been determined by considering a pixel noise of $220e^-$ and a spread of the discriminator thresholds of $160e^-$, as reported in [1].

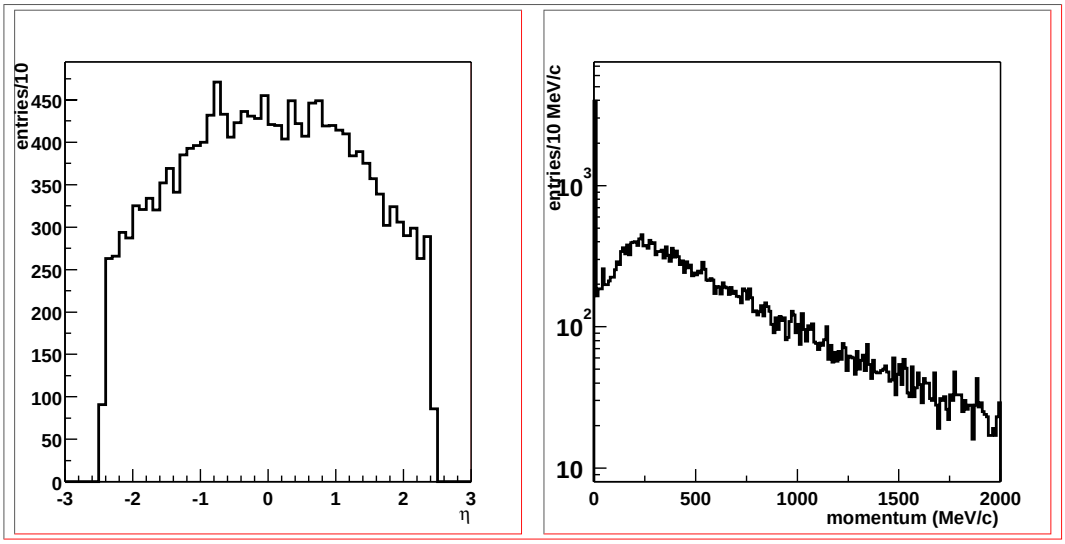

Figure 2: *Pseudorapidity (η) distribution of primary charged particles and momentum distibution of tracks crossing the SPD layers, including δ-rays produced in the detector.*

We have already studied that F_r and F_c play no role with respect to δ-rays.

As a first prediction of the model, we calculated the digit multiplicity. The average number of digits per ladder is 467 for layer 1 and 254 for layer 2. Considering that each ladder contains 256×192 pixels cells, the resulting occupancy is, for layer 1 and layer 2, respectively 0.95% and 0.52%. In section 5.3 the dependence of the digit multiplicity on the number of generated tracks will be analysed.

In fig. 3 the column (x coordinate) and row (z coordinate) cluster length distributions are shown for both layers. Diagonal clusters are also considered. It can be noted that, due to the turbo geometry, the average x cluster length is larger in the second layer, where most of the clusters have length equal two.

In order to determine the resolution of the detector, we calculate the variables:

$$\begin{aligned} D_x &= x_{sp} - \frac{x_{in} + x_{out}}{2} \\ D_z &= z_{sp} - \frac{z_{in} + z_{out}}{2} \end{aligned} \qquad (2)$$

where $x_{sp}(z_{sp})$ is the x (z) coordinate of the space point of the cluster, as previously defined, and x_{in} (z_{in}) and x_{out} (z_{out}) are the coordinates of the entrance and exit hits of the track associated to the cluster. In fig. 4 the distributions of D_x and D_z are reported for both layers.

All the distributions are fitted with a Gaussian, whose mean value and standard deviation are reported in the same figure. The fitted standard deviation is a

measure of the resolution and is better in the first layer for x direction and in the second layer for z, depending on the relative cluster size. It should be noted that the distributions are not really Gaussian and they seem to have a more complex structure. The D_x distributions, in particular, are fitted with a very bad χ^2.

An insight into this problem can be gained by plotting D_x and D_z versus the cluster size in the corresponding direction. In fig. 5 these plots are reported on the left, for both layers. We notice that most of the clusters have lengths less than three and their D_x and D_z variables do not exceed half the length of the pixel in the corresponding direction. However, on the tails of the scatter plots there are also few points which seem to follow a double structure: some clusters have a large length, but small values of D, whereas some clusters show an increase of D with the cluster size.

In section 5.1 (fig. 11) we will show the D_x variable as a function of the impact angle of the track associated to the cluster, for layer 1 (left) and layer 2 (right). A double structure is present also in these plots and we can notice that the first group correspond to tracks with a very large impact angle, while the second group corresponds to tracks with small angles, typical to the tracks coming from the target. Tracks with large impact angles can be introduced by physical effects, which generates secondaries and δ-rays. In addition, the geometrical charge sharing mechanism can associate these tracks to clusters with large length and consequently small D, since tracks firing more pixels give more spatial information. To verify this, we have performed a special simulation at the same primary track multiplicity, but with all the physical effects, including δ-ray production, switched off. In fig. 6 are shown, for layer 1, the scatter plots of D_x and D_z versus the cluster length in the corresponding directions, using the results of the special generation. Comparing this figure with the corresponding plots of fig. 5, one can notice that the points of the first group, at large cluster length and small D, have disappeared, as expected.

Nevertheless, the points belonging to the second group, having D correlated with the cluster length, are still present in this simulation. A detailed analysis, performed on both simulations, allows us to conclude that these clusters are formed by pixels fired by more than one primary track. In this case, the cluster has a large cluster length and also a bad resolution, since only one primary track is considered in the computation.

The scatter plots on the left of fig. 5 have been fitted with a Gaussian distribution in each bin of the corresponding cluster length. The fitted standard deviations are plotted on the right of the same figure, which therefore shows the x and z resolutions as a function of the corresponding cluster length. The horizontal lines represent the resolutions obtained by the global fit of fig. 4. As we can see from the figure, the global resolutions are mostly determined by the clusters with length 1; for cluster of length 2 the resolution is better, but afterwards, for clusters with length greater than 3, the contribution from clusters formed by more than one track becomes dominant and the resolution is worse again. A

different behaviour is followed by the D_x distribution of layer 2, where the turbo geometry plays a major role. Here most of the clusters have length 2 and they give the leading contribution to the resolution determination.

In fig. 7 the errors on the space points, as defined in (1), are shown as a function of the cluster length, in both x and z directions. The layer 1 and layer 2 are considered together in this figure. A square root dependency of the errors on the cluster length is clearly visible in the plot relative to the x direction, as expected from expression (1).

It can be noted that in both plots several values of the space point error are associated to a given bin of the cluster length, each one corresponding to a different cluster configuration. For the first bin, in particular, there is a single value of the error in x direction (50 μm/$\sqrt{12}$) and two values in z direction, one for normal columns (425 μm/$\sqrt{12}$) and the other for special columns (625 μm/$\sqrt{12}$).

The main results are summarized in the following table, where the average occupancy, cluster size and resolution are reported for both layers 1 and 2.

Table 1: Summary of the main simulation results obtained at a pseudorapidity density of 4500 charged particles at central η.

	Layer 1		Layer 2	
Occupancy (%)	0.95		0.52	
	x	z	x	z
$\langle$Cluster size$\rangle$	1.56	1.48	2.24	1.32
Resolution (μm)	11.1	97.7	11.5	93.9

In the following we will study these results as a function of the track impact angles, the parameters of the model and the primary particle multiplicity.

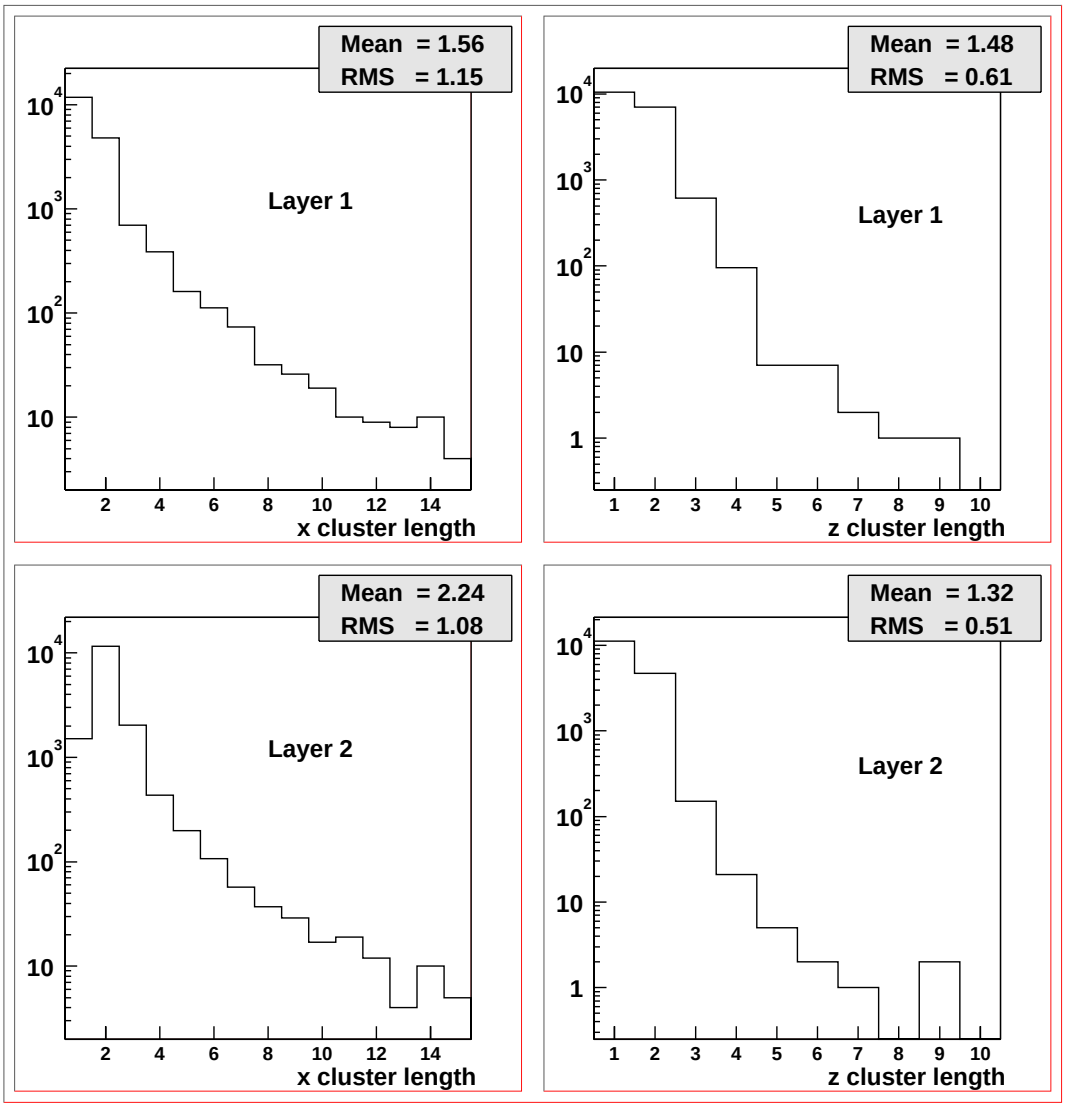

Figure 3: *Cluster length distributions in x (column) and z (row) directions, for layer 1 and layer 2.*

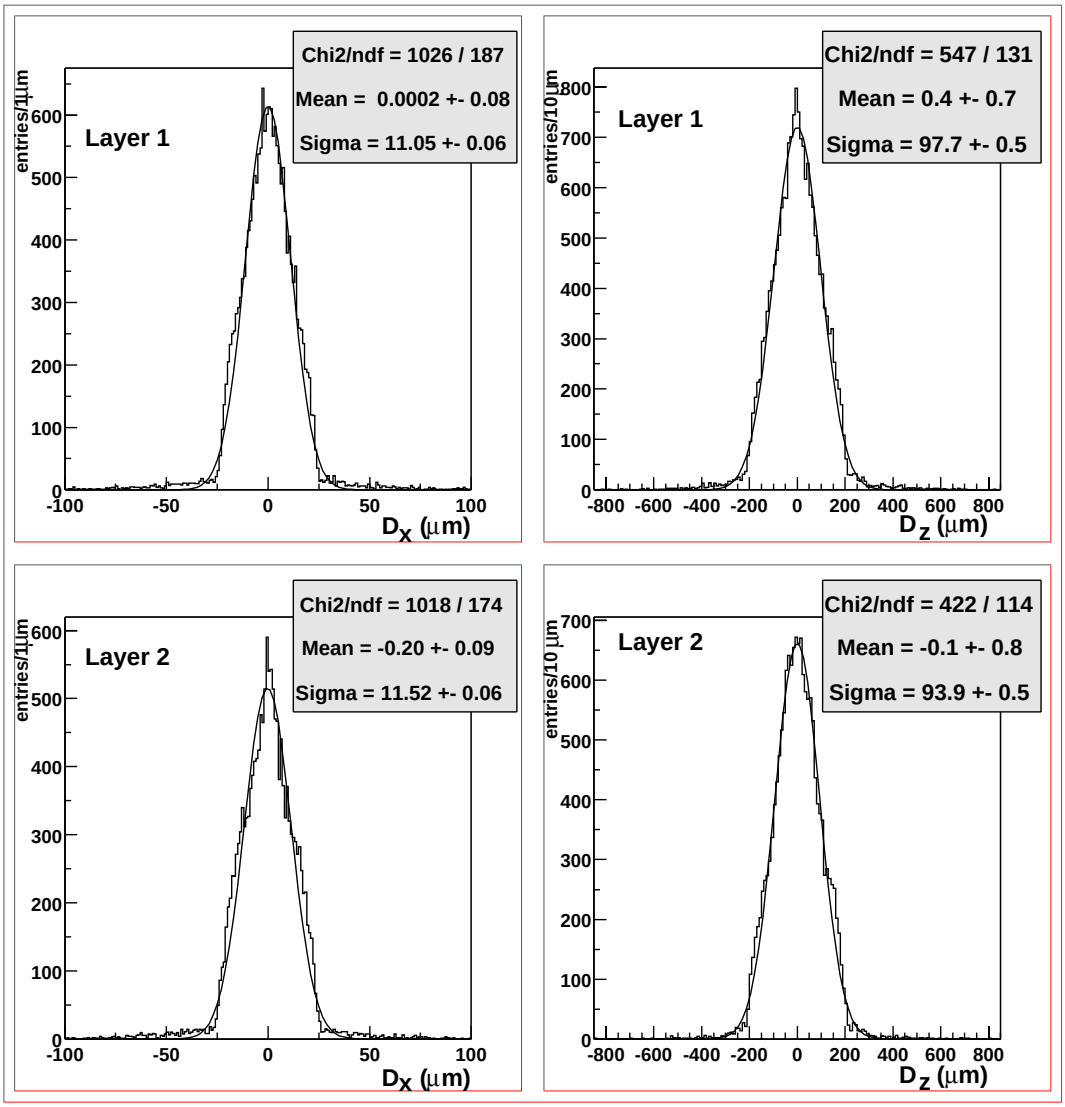

Figure 4: *Distribution of the D_x and D_z variables for both layers. In full line and in the boxes are reported the results of a Gaussian fit. The standard deviation Sigma measures the resolution of the detector.*

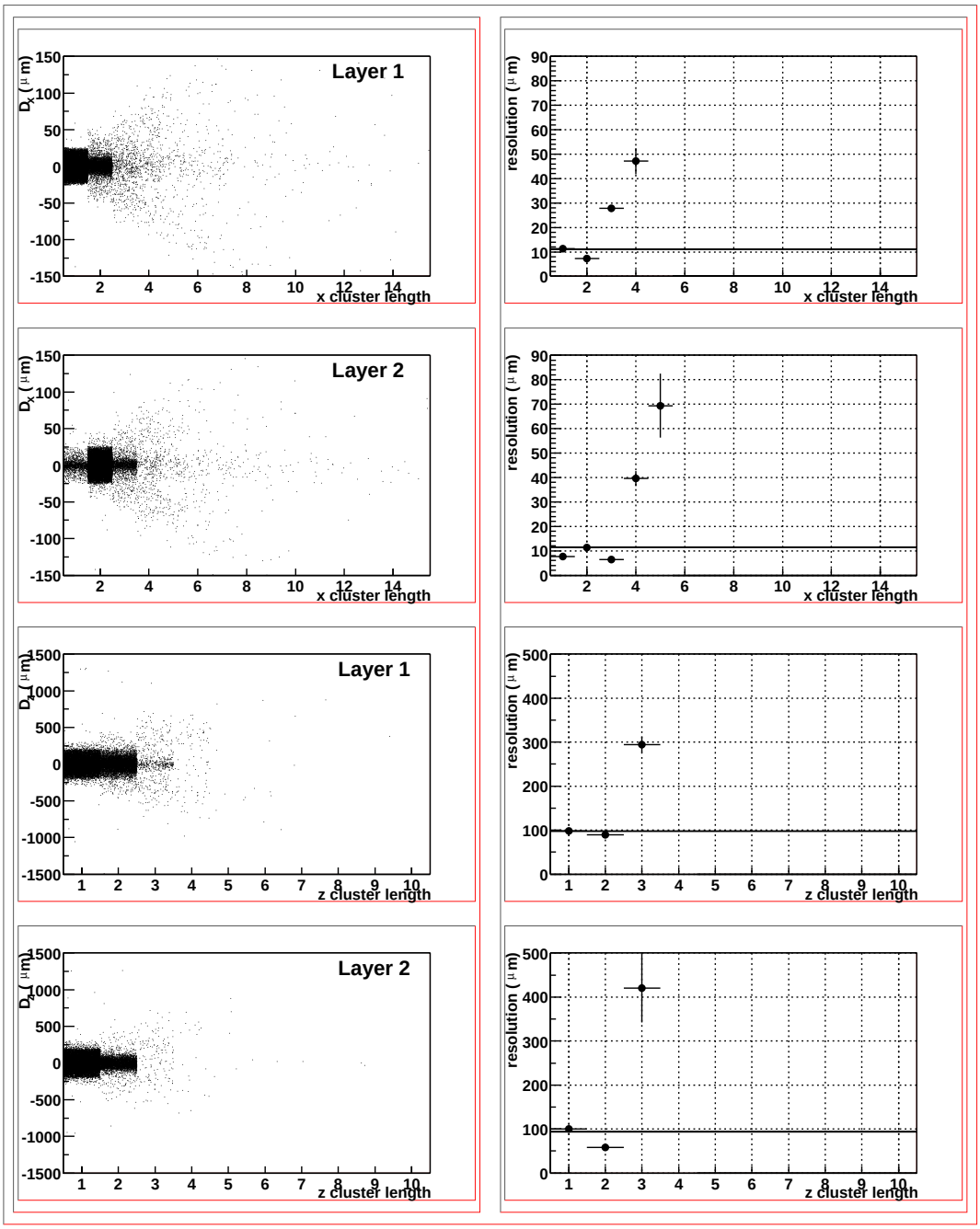

Figure 5: *Left: scatter plot of the D_x and D_z variables versus respectively the x and z cluster length, for both layers. Right: x and z resolution as a function of the x and z cluster length respectively, for both layers. The full line shows the resolution obtained by a global fit.*

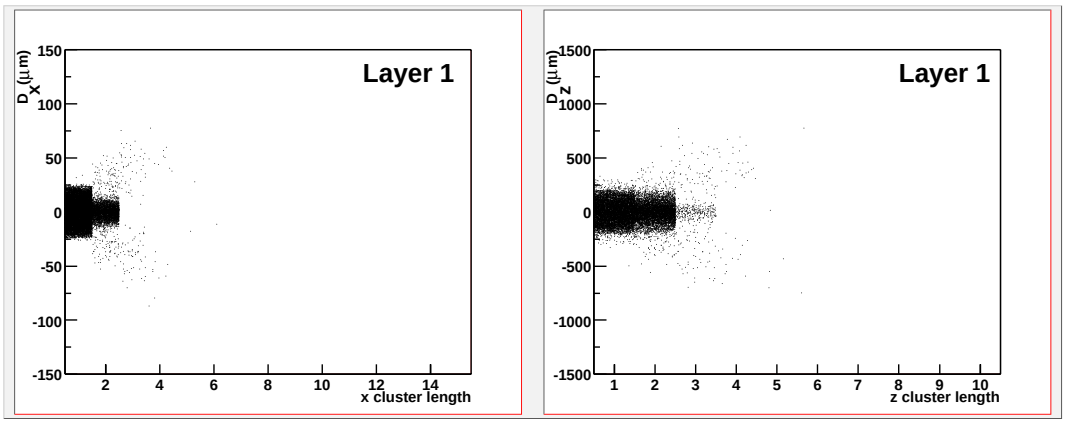

Figure 6: *Scatter plot of the D_x (left) and D_z (right) variables versus respectively the x and z cluster length, for layer 1. All the physical effects, including δ-rays production, are switched off.*

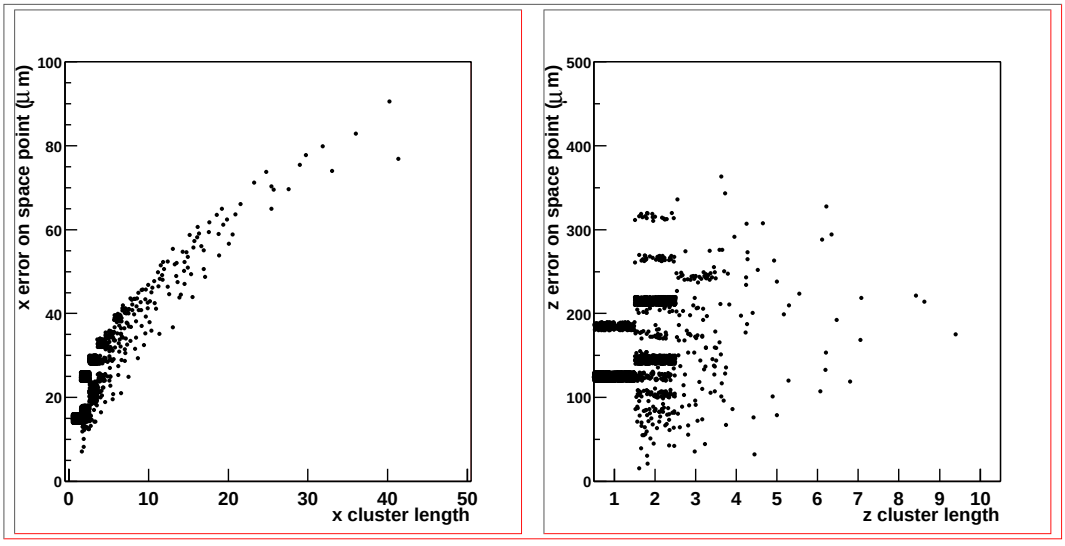

Figure 7: *x and z errors associated to the space points. Ladders from layer 1 and layer 2 are considered together.*

5.1 Dependence on the track impact angles

We define the angles ϕ and λ as the impact angles of a track with respectively the zy and xy planes of the pixel detector, where the y direction is perpendicular to the pixel planes.

The ϕ and λ angle distributions for both layers are shown in fig. 8. The bins with higher contents corresponds to the impact angles of the primary tracks and defines the angular range covered by the detector for tracks coming from the target. While a large coverage of the λ angle is present in the z direction, where four ladders are aligned in the stave along their longer side, only a small interval of the ϕ angle is accepted in the x direction. In the first layer the tracks have $\langle\phi\rangle = 3.6°$, since the staves are almost perpendicular to the radial direction, while in layer 2 the average value of the track ϕ angle is $\langle\phi\rangle = -21.4°$, due to the turbo geometry.

The distributions of D_x and D_z for both layers, as a function of the ϕ and λ angles are shown on the left of fig. 9. In the scatter plots the angle ranges have been chosen in orded to show only the most populated regions. It can be seen that the resolution is worst for zero angle values (perpendicular incident tracks).

The D_x and D_z distributions were fitted with a Gaussian in slices of the corresponding track impact angles. The resulting standard deviations are reported on the right side of the same figure, where the ideal values (pixel length)/$\sqrt{12}$ are shown as dashed line for comparison. The fitted values are in agreement with the ideal ones at zero angle, i.e. in the worst case. In full line are reported the resolutions obtained by the global fit, as shown in fig. 4.

A better understanding of the shape of the correlations shown in fig. 9 can be reached by considering the cluster length. On the top of fig. 10 are reported the D_x distributions versus the ϕ angle for clusters of length 1 (left) and length 2 (right) in x direction. On the bottom of the same figure the D_z distributions versus the λ angle for clusters of length 1 (left) and length 2 (right) in z direction are reported. Only the layer 1 is considered in these plots. It can be seen that the correlations on the left side look completely different from those on the right side; the two trends are overimposed in the plots of fig. 9. The shape of the correlations for clusters of length 1 can be explained in the following way: consider a single fired pixel of thickness h and length Δx and Δz respectively in x and z directions. In this case the space point has coordinates ($x_{sp} = \frac{\Delta x}{2}$, $z_{sp} = \frac{\Delta z}{2}$), by referring to one side ot the pixel. The resolution is worse if a track has zero impact angle and is at one side of the pixel. As the impact angle increases, the resolution is better and better. Therefore, considering the definitions (2), the curves limiting the points in the correlations on the left of fig. 9 can be described *via* the following functions:

$$|D_x| = \frac{1}{2}(\Delta x - h \tan\phi)$$

$$|D_z| = \frac{1}{2}(\Delta z - h \tan\lambda) \qquad (3)$$

On the other hand, the clusers with length 2 have the space point at coordinates ($x_{sp} = \Delta x$, $z_{sp} = \Delta z$), by referring to one side of the cluster. In this case a track at zero impact angle cannot be at one side of the cluster, since it has to cross the two pixels anyway. Therefore, the curves limiting the correlations on the right of fig. 10 can be described by considering a track at zero impact angle in (x_{sp}, z_{sp}), which spans the angles ϕ and λ worsening the resolution. The functions are in this case:

$$\begin{aligned} |D_x| &= \frac{h}{2}\tan\phi \\ |D_z| &= \frac{h}{2}\tan\lambda \end{aligned} \qquad (4)$$

The full lines in fig. 10 refers to eq.(3) and (4) and have been drawn using the nominal values $\Delta x = 50\ \mu m$, $\Delta z = 425\ \mu m$ and $h = 150\ \mu m$. They describe fairly well the shapes of the correlations. In addition, in the plot on the bottom left of the same figure, where the D_z variable is considered for clusters of length 1 in z direction, the detailed chip structure of the pixels is visible, with the larger sized pixels at the end of each chip producting an anomalous increase of the resolution.

In fig. 11 the scatter plots of the D_x variable versus the ϕ angle are shown with a full angle coverage, both for layer 1 (left) and layer 2 (right). In both plots a clear separation between large ϕ - small D_x and small ϕ - large D_x is visible, as already reported. The points at large ϕ and small D_x belong to very tilted tracks, producing clusters with a great size due to charge sharing. They are associated to small values of D_x, hence to well reconstructed space points. On the other hand, the points at large D_x fall in the range of ϕ proper of the primary tracks. As already argued, they are due to clusters formed by more than one primary track. In this case the resolution can be worsened by adding digits to the cluster not correlated to the direction of the track associated to the cluster.

The dependence of the cluster size from the impact angles can be studied in fig. 12. Here the x and z cluster lengths for layer 1 are reported as a function of the absolute value of the difference between the corresponding coordinates of the entrance and exit point of the track. These latters are proportional to $\tan(\phi)$ and to $\tan(\lambda)$, respectively. A clear correlation, especially in x direction, can be seen. As deduced from fig. 11 and fig. 5, this is due to the geometrical charge sharing, while the δ-rays and the clusters formed by more than one primary track introduce points at small angles, not correlated to the cluster size.

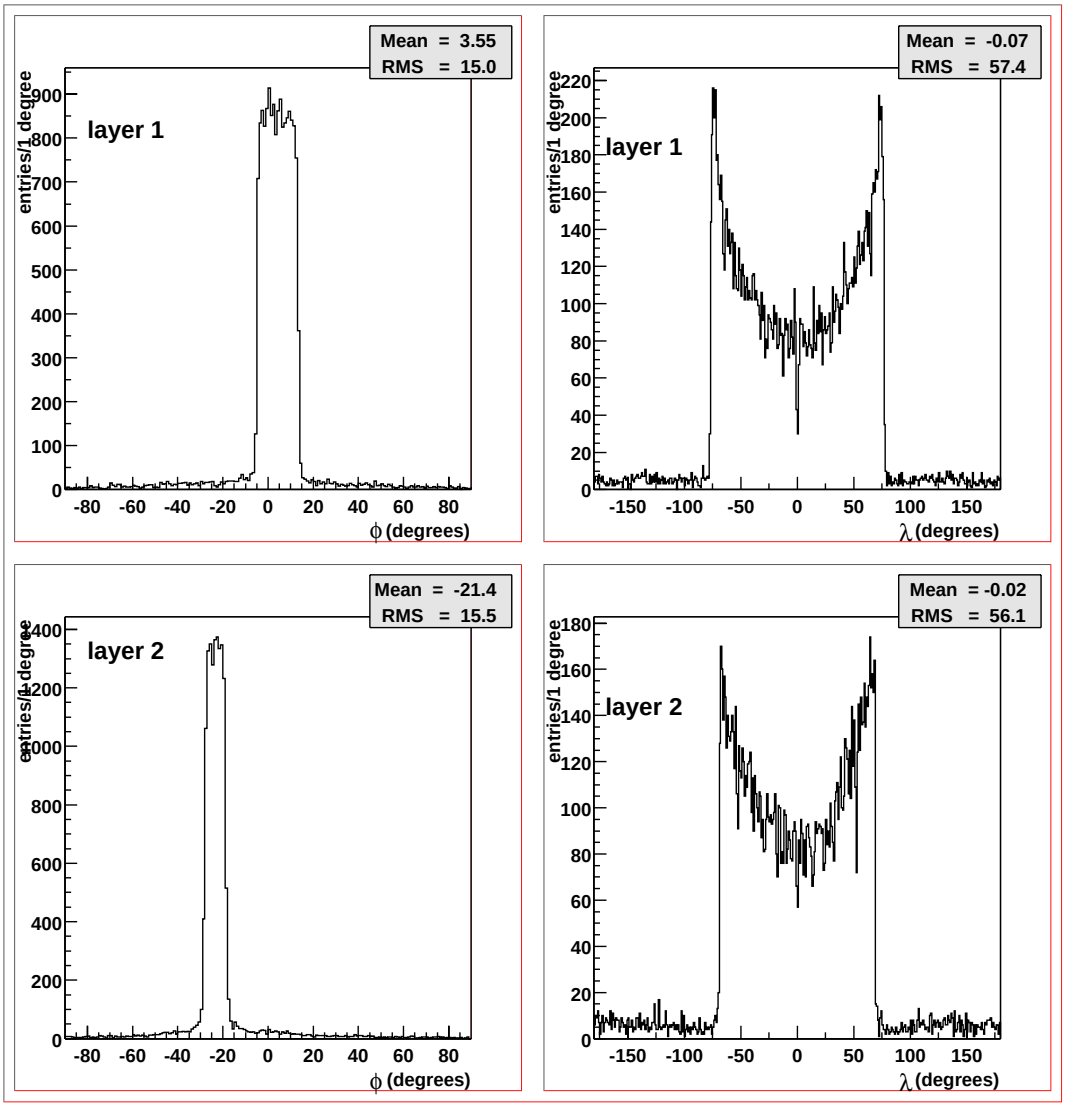

Figure 8: *Distributions of impact angles of the particles on the pixel detectors.*

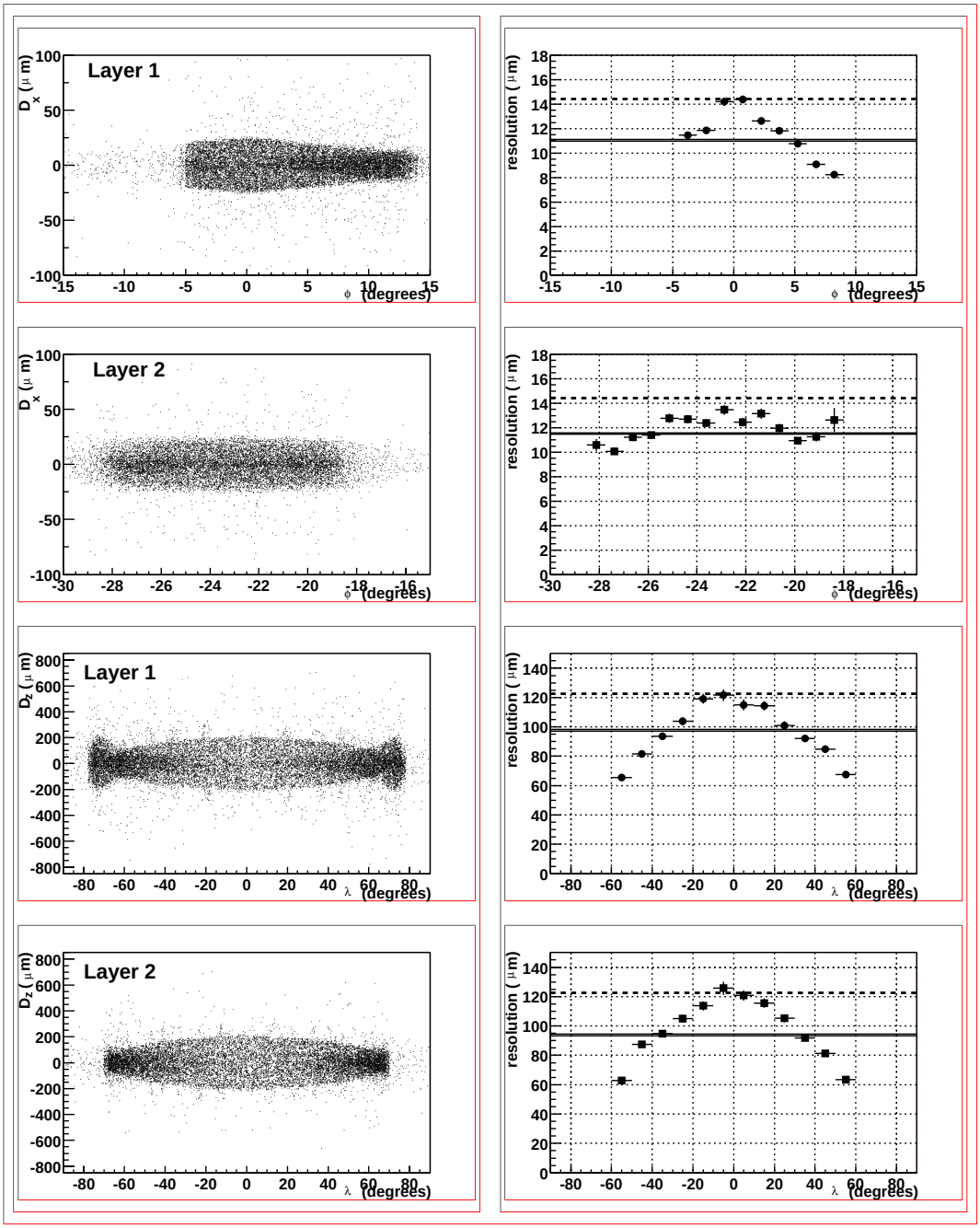

Figure 9: *Left: scatter plot of the D_x and D_z variables versus respectively the ϕ and λ impact angles, for both layers. Right: x and z resolution as a function of the ϕ and λ impact angles respectively, for both layers. The full line shows the resolution obtained by a global fit, the dashed line corresponds to the expected values for the resolution of a single pixel.*

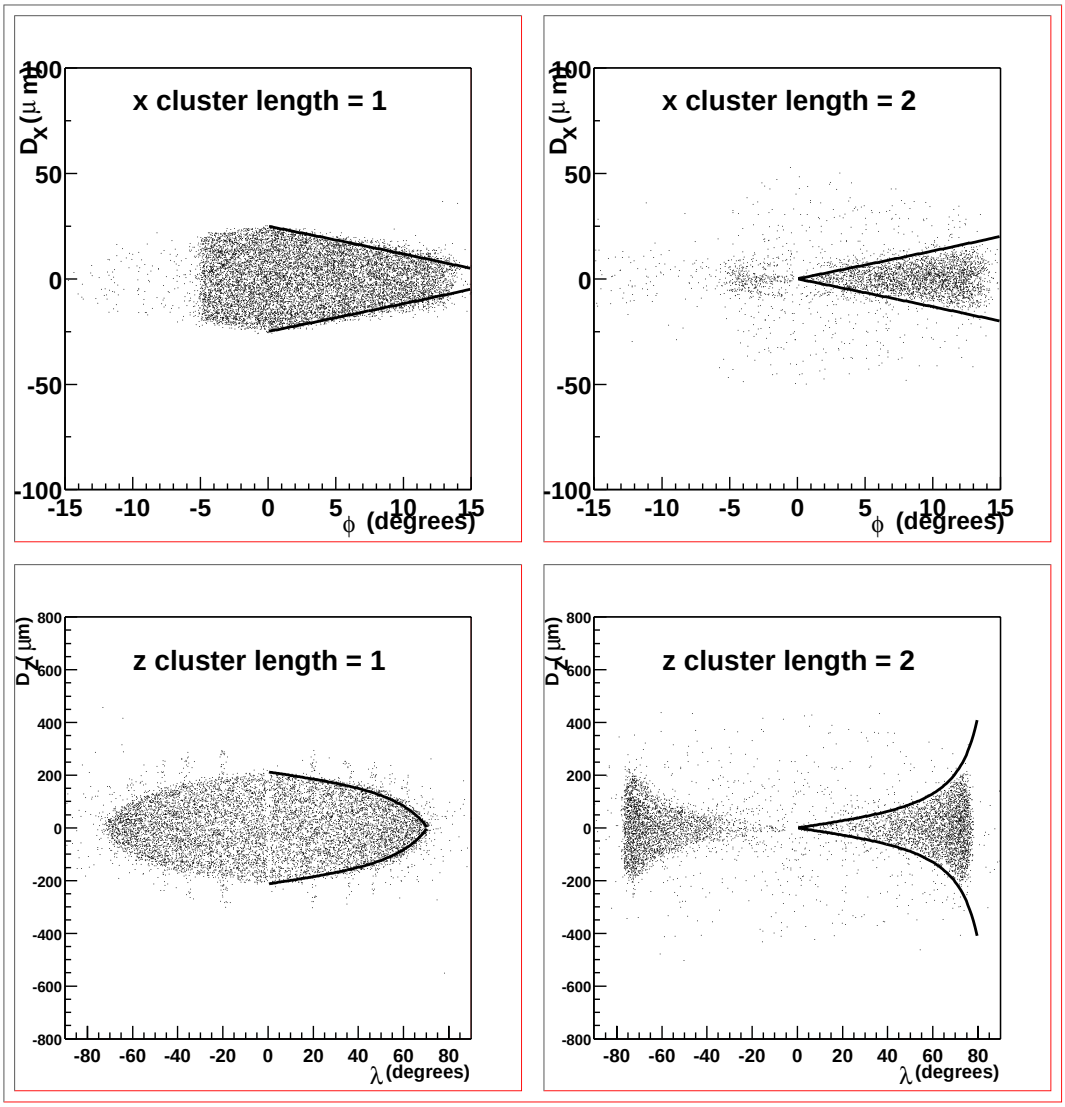

Figure 10: *Top: scatter plots of the D_x variable versus the ϕ impact angle for clusters of length 1 (left) and of length 2 (right) in x direction. Bottom: scatter plots of the D_z variable versus the λ impact angle for clusters of length 1 (left) and of length 2 (right) in z direction. Only the layer 1 is considered.*

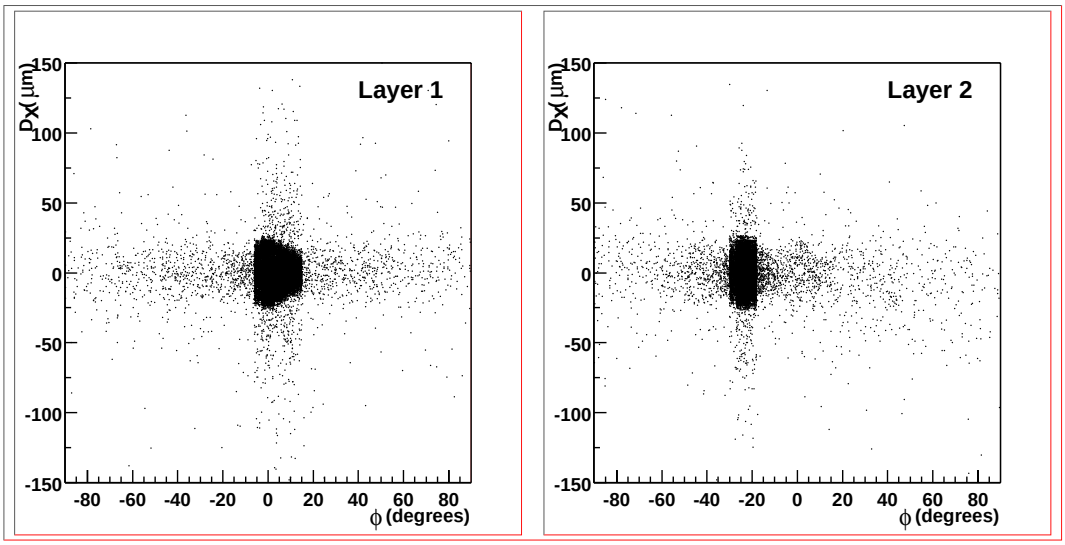

Figure 11: *Scatter plots of the D_x variable versus the ϕ impact angle for layer 1 (left) and layer 2 (right) The full angle coverage is considered.*

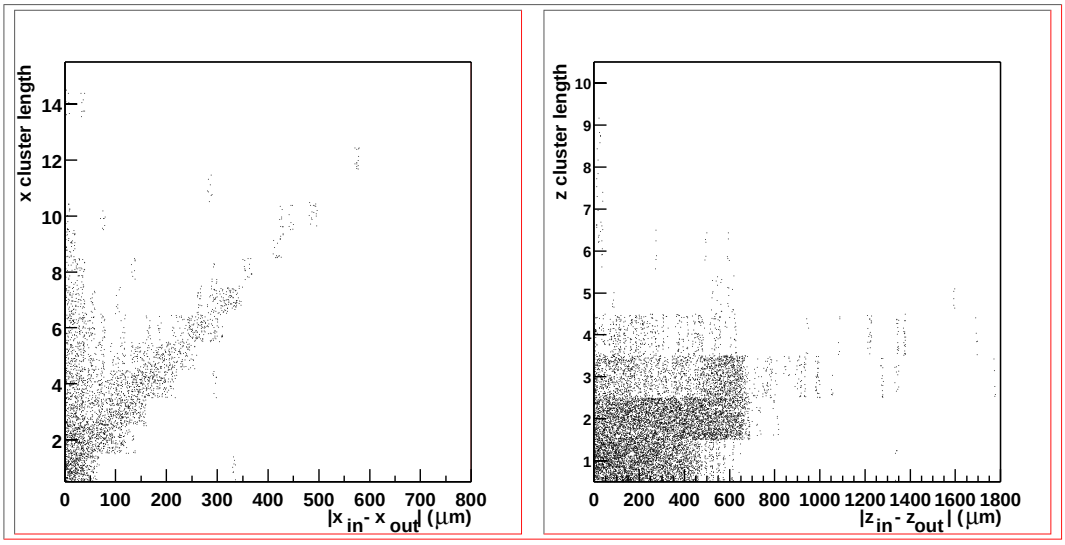

Figure 12: *x and z cluster lengths as a function of the absolute value of the difference between the corresponding coordinates of the entrance and exit hits. Only the layer 1 is considered.*

5.2 Dependence on the parameters of the model

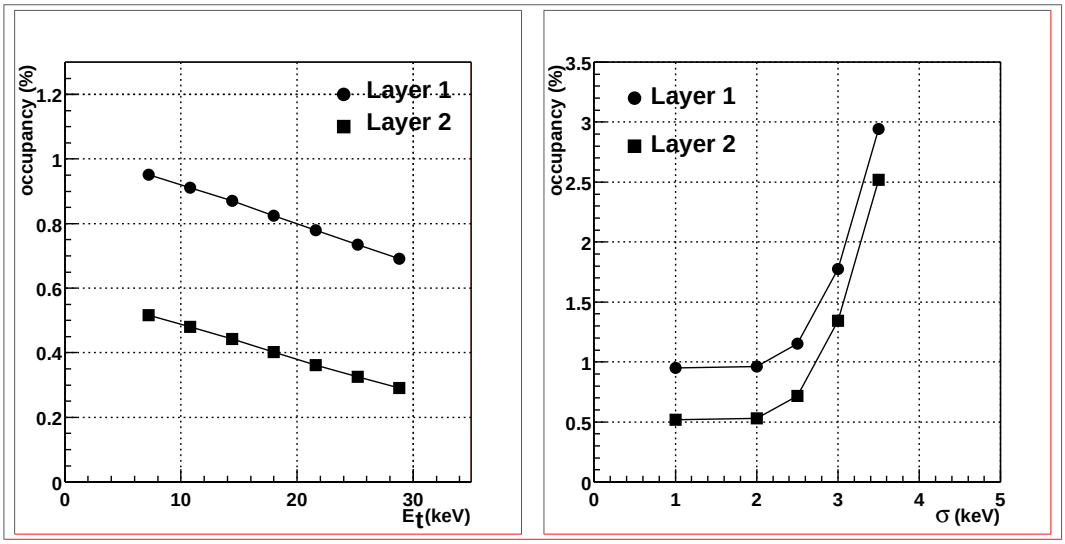

Figure 13: *Occupancy of layer 1 and layer 2 as a function of the E_t parameter (left) and of the σ parameter (right).*

In the following the sensibility of the simulation results to the settings of the E_t and σ parameters are studied.

In fig. 13 the occupancies for both layers as a function of the threshold E_t and of the fluctuation parameter σ are reported. As already discussed in [3], the increase of the threshold results in a decrease of the total number of digits, hence in a decrease of the occupancy. Moreover, this number is highly sensitive to the noise level, if the σ parameter is greater than 2 keV, corresponding to $\sim 30\%$ of the threshold value.

In fig. 14 and fig. 15 the average cluster sizes of both layers, respectively in x and z direction, are reported as a function of E_t and σ; the same scale is used in both figures. The increase of E_t produces a decrease of the cluster sizes, as for the occupancy discussed before. The increase of the noise results in an increase of the clusters of length 1 and in a decrease of the average cluster sizes for $\sigma > 2$ keV. It can be noted that in the x direction, due to the turbo geometry, the layer 2 has a greater sensitivity to changes of the E_t and σ parameters than the layer 1. On the other hand, the two layers exhibit the same variation with the parameters of the model in z direction, where they have similar impact angles for the incident tracks.

In fig. 16 the resolution (measured by the standard deviation of the Gaussian fitted to the D_x and D_z distributions) is shown as a function of E_t. As E_t is increased, the cluster information is reduced and resolution worsens slowly. The x resolution of layer 2 shows a change in shape that can be explained by the following argument. As E_t is increased, the clusters with length 1 are enhanced

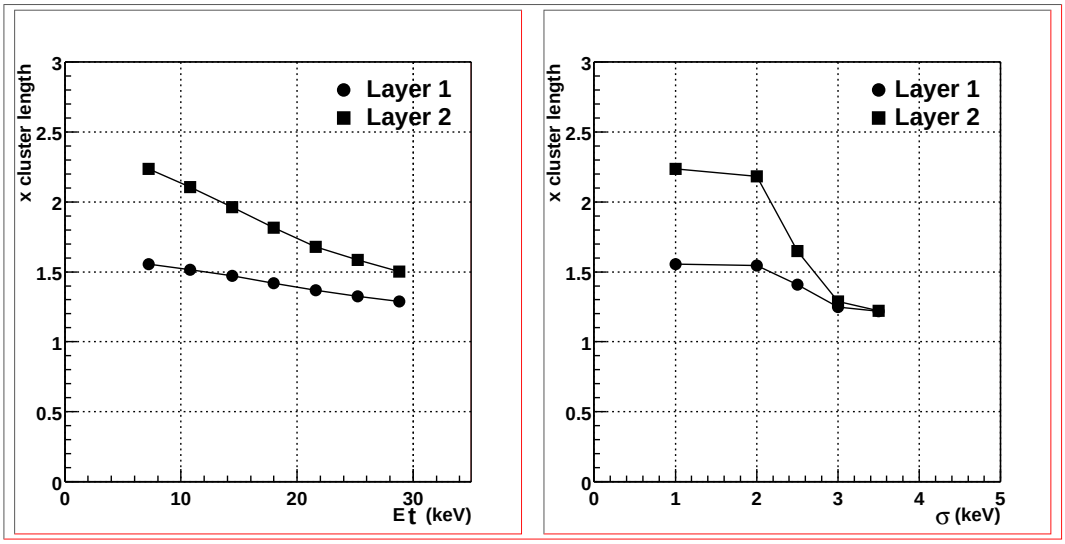

Figure 14: *Average x cluster length of layer 1 and layer 2 as a function of the E_t parameter (left) and of the σ parameter (right).*

with respect to those with higher length. In fig. 5 (left side) we can see that an increase in the number of clusters with length 1 can improve the resolution only for the layer 2 in x direction, where the turbo geometry introduces a different trend. For higher values of E_t, however, the number of clusters having length equal 3 in x direction gets negligible also for this layer, therefore the resolution becomes worse.

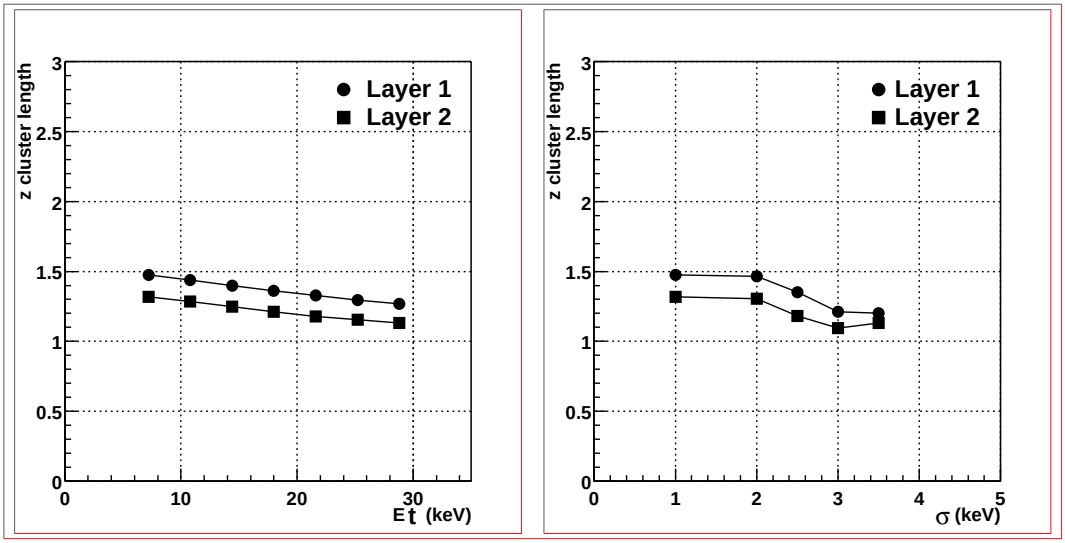

Figure 15: *Average z cluster length of layer 1 and layer 2 as a function of the E_t parameter (left) and of the σ parameter (right).*

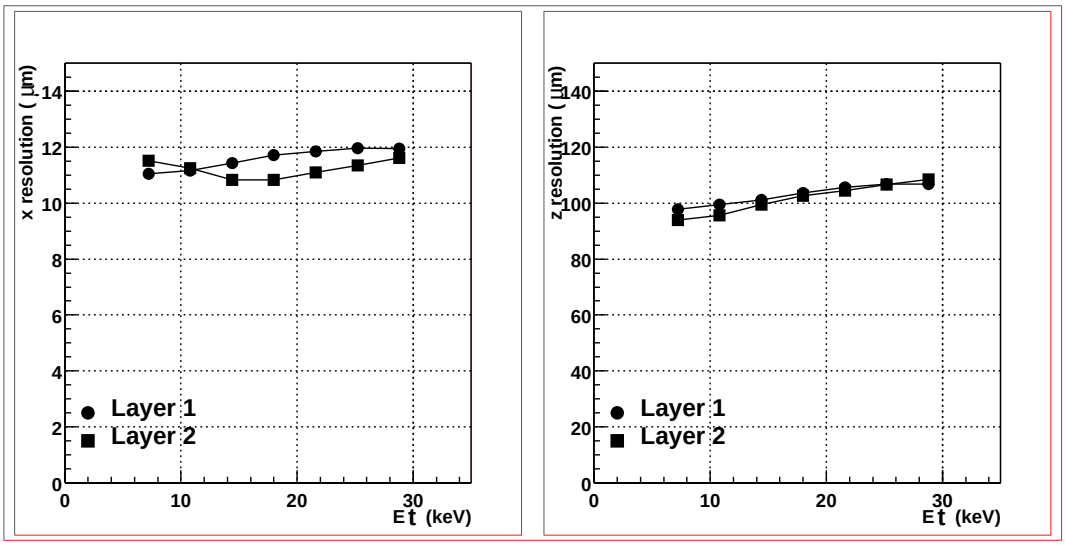

Figure 16: *Resolution of layer 1 and layer 2 in x (left) and z (right) as a function of the E_t parameter.*

5.3 Dependence on the particle multiplicity

For this study the E_t and σ parameters were again fixed to their nominal values.

In fig. 17 the occupancies for each layer as a function of the number of primary charged particles per unit of pseudorapidity at central η ($\frac{dN}{d\eta}$) are shown. The value $\frac{dN}{d\eta} \sim 4500$ corresponds to the value used for the previous analysis. The trend is fully linear in the considered multiplicity range, both for layer 1 and layer 2. Comparing with [1], we observe that the occupancy of layer 2 is enhanced with respect to the occupancy of layer 1. This is due to the introduction of the geometrical charge sharing and to the larger x cluster length in layer 2.

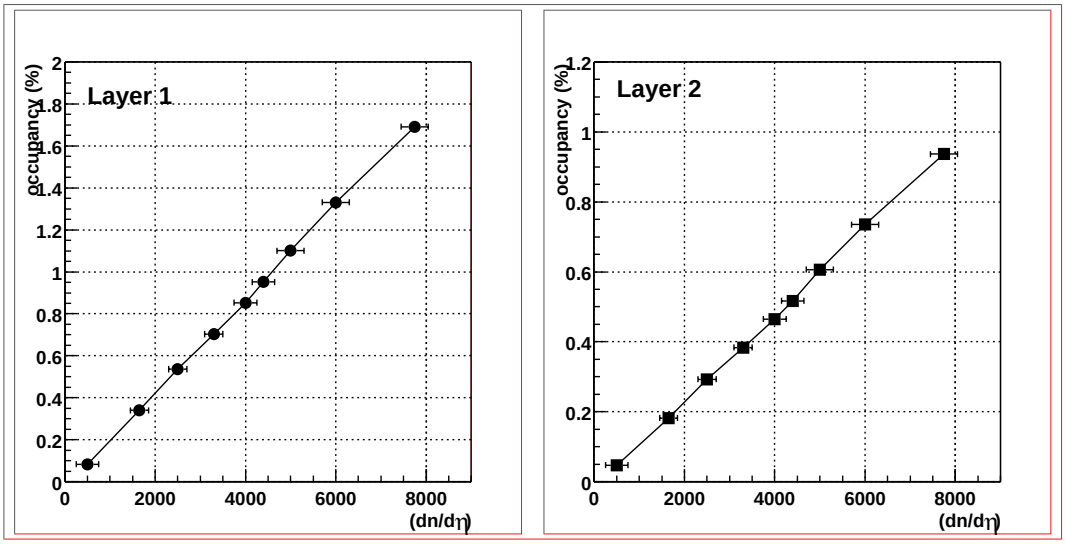

Figure 17: *Occupancy of layer 1 (left) and layer 2 (right) as a function of the primary charged particles per unit of pseudorapidity at central η.*

The cluster sizes and the resolutions have been found to be almost independent on the particle multiplicity, in this limit of low occupancy.

Moreover, we have verified that the dipendency of the occupancy with the values of the E_t and σ parameters has the trend shown in fig. 13, regardless of the multiplicity used in the considered range.

6 Conclusions

We have presented the results of the simulation of the response of the ALICE silicon pixel detector to minimum ionizing particles. Events were generated with the HIJING parametrization, and traced in the full ITS with AliRoot.

Average occupancies, cluster lengths and resolutions have been evaluated in different conditions of multiplicity. The dependencies on the track impact angles and on the parameters of the slow simulation model have been investigated as

well. We have shown that the occupancy is below 1% for layer 1 and about 0.5% for layer 2 at $\frac{dN}{d\eta} \sim 4500$, provided the contribution of the noise and of the spatial dispersion of the discriminator threshold is kept below the 30% of the mean threshold value.

At the highest considered multiplicity, namely $\frac{dN}{d\eta} \sim 8000$, the occupancy is below 1.8% for layer 1 and 1% for layer 2, under the same assumption.

The parameters of the model have been set according to the corresponding nominal values of the new ALICE1 chip. A new calibration of the parameters should be performed as soon as experimental data from test beams on the new ALICE chip will be available.

References

[1] ALICE Collaboration, ALICE TDR 4, CERN/LHCC 99-12. (1999).

[2] ALICE Collaboration, Technical proposal, CERN/LHCC 95-71 (1995).

[3] R. Caliandro et al., ALICE internal note INT-00-23, 12 September2000.

[4] V. Manzari et al. J.Phys. **G 25** (1999) 473.

[5] see http://www1.cern.ch/ALICE/Projects/offline/aliroot/Welcome.html.

[6] R. Brun and F. Rademakers, Nucl. Instr. and Meth. in Phys. Res. **A 389** (1997) 81-86.

[7] R. Caliandro et al., "Simulation of the response of a silicon pixel detector", submitted to Nucl. Instr. and Meth. in Phys. Res. A.

[8] R. Dinapoli et al., "An analog front-end in standard 0.25 μm CMOS for silicon pixel detectors in ALICE and LHCb", CERN/LHCC/2000-041, 110-114.